CEAS Aeronautical Journal (2022) 13:967–977
https://doi.org/10.1007/s13272-022-00615-0

ORIGINAL PAPER

# Aeroelastic-tailoring of a wind-tunnel model for passive alleviation of static and dynamic loads

Nicolò Fabbiane[1] · François-Xavier Irisarri[2] · Johannes Dillinger[3] · Arnaud Lepage[1]

Received: 28 March 2022 / Revised: 22 August 2022 / Accepted: 23 August 2022 / Published online: 24 September 2022


**Abstract**
Composite materials allow to tailor the elastic properties of a structure. In aeroelasticity, this opens up the possibility to passively enhance the coupled aerostructural characteristics. In this work, the design of a composite wing is addressed with the aim to alleviate static and dynamic aeroelastic loads; these two objectives are quantified by the root-bending-moment in a high load-factor condition and the deformation amplitude of the wing under gust. A two-step approach of the optimal design of the structure is adopted. A Pareto front is computed via an aeroelastic model of the wing; the aerodynamic loads are modelled, depending on the load-case, either via the DLM or the RANS equations. The best-compromise design is chosen via a criterion based on the jig-shape and, finally, the stacking-sequences are computed via a specialised evolutionary algorithm.

**Keywords** Aeroelastic tailoring · Passive load-alleviation · Gust response · Composite materials · Bi-objective optimisation

## 1 Introduction

Aeroelastic-tailoring can be defined as "the embodiment of directional stiffness into an aircraft structural design to control aeroelastic deformation, static or dynamic, in such a fashion as to affect the aerodynamic and structural performance of that aircraft in a beneficial way" [1]. The first example of this technique can be traced back to Munk's patent in 1949 on the use of the natural anisotropy of wood to control the deformation of a propeller [2].

The advent of composite materials, and the advances in their manufacturing and mastery, allowed more and more to control static and dynamic behaviours of structures and, thus, the coupling with aerodynamic forces [3, see for an extended and exhaustive historical review]. Composite laminates are intrinsically discrete due to their layered nature. This, with the large number of design variables given by the plies orientation, leads to a complex combinatorial optimisation problem, for which evolutionary (or genetic) algorithms are an efficient solution both in pure structural mechanics [4] and aeroelasticity [5]. Nevertheless, this approach can be costly due to the large number of structural evaluations needed to converge to an optimised design. A solution to this issue is given by homogenisation techniques applied to the composite behaviour that allows to represent the mechanical properties of a composite plate with a reduced set of continuous parameters at the expense of loosing the detailed information on the stacking sequence of the plies [6, 7]. This reduced design space allows for more computationally efficient approaches to aeroelastic tailoring [8, 9], where the complete stack information is reconstructed a-posteriori by the solution of an inverse problem [10, 11]. This approach remains deterministic and does not take into account the uncertainties linked to the manufacturing process of composite materials: in recent years, steps have been made in

François-Xavier Irisarri, Johannes Dillinger, and Arnaud Lepage are contributing authors.

✉ Nicolò Fabbiane
nicolo.fabbiane@onera.fr

François-Xavier Irisarri
francois-xavier.irisarri@onera.fr

Johannes Dillinger
johannes.dillinger@dlr.de

Arnaud Lepage
arnaud.lepage@onera.fr

[1] DAAA, ONERA, Université Paris-Saclay, 29 av. de la Division Leclerc, 92322 Châtillon, France

[2] DMAS, ONERA, Université Paris-Saclay, 29 av. de la Division Leclerc, 92322 Châtillon, France

[3] Institute of Aeroelasticity, DLR, Bunsenstr. 10, 37073 Göttingen, Germany

this direction by investigating stochastic and reliable optimisation techniques applied to aeroelastic tailoring [12, 13].

From the aerodynamic point of view, the fluid has been historically modelled as a potential flow [14, 15], allowing for a fast and reliable evaluation of the aerodynamic generalised forces. However, this is true when the flow is *well behaved* (attached boundary layer, no flow-separation, ...) and at subsonic speeds; with the advent of transonic airplane, the interest for a more accurate representation of the flow became of interest. Reynolds-Averaged Navier-Stokes (RANS) equations have been recently introduced in the optimisation loop as an high-fidelity representation of the flow dynamic in aeroelastic and aerostructural design problems [16–18].

This work is part of a common research project between ONERA and DLR that aimed to study the dynamic aeroelastic behaviour of a flexible composite wing, from its design to its characterisation by means of wind-tunnel aeroelastic tests. The project focused on the consolidation of already available deterministic, potential-flow, aeroelastic design techniques to design two wings—one for each institution—to passively alleviate gust-loads, while ensuring the integrity of the model. The design of the two wings had been finalised in mid-2019 to be manufactured at DLR and the campaign of aeroelastic wind-tunnel tests successfully took place at ONERA in the first semester of 2021. The latter aimed to characterise the aeroelastic behaviour of the models in static and dynamic conditions, thanks to gust-generators at the inlet of the test-section [19–21]. As well as conventional punctual pressure and acceleration measurements [22, 23], combined pressure-sensitive-paint (PSP) [24, 25] and model-deformation-measurements (MDM) [26] were performed on the suction side of the wings; these techniques allow for a deeper characterisation of the link between structure and aerodynamics and a more extensive comparison against the numerical simulations. The objective of this work is to present a complete aeroelastic optimisation method of a composite wing, as applied to the wind-tunnel model designed by ONERA.

The article is organised as follows. After a brief introduction to the wing-geometry, optimisation variables, and parameters (Sect. 2), the optimisation procedure and the sizing load-cases are discussed (Sect. 3). The optimal design-points are presented in the form of a Pareto-front and, between them, the final design is chosen (Sect. 4). Finally, the stacking-sequence is computed and its performance verified (Sect. 5).

## 2 Application case

The geometry is based on the Common Research Model [27]; the flight-shape used in the model-design is obtained by scaling the CRM geometry to a root-to-tip span equal to 550 mm, resulting in a root chord and reference surface of approximately 248 mm and 729 $cm^2$.

The structural configuration of the wing is given by two composite skins- upper and lower-, filled by a polymeric foam; the simplicity of this configuration has been chosen to ease the manufacturing process, due to the small size of the model. The material of choice for the wing-skin is a glass-fiber/epoxy composite with a fiber volume-fraction equal to 0.39; a standard low-density polymeric foam is instead adopted for the filling, see Table 1. The uni-directional composite ply is considered as an orthotropic material with its first principal direction oriented as the fibers; the thickness of a single ply is 0.17 mm and it can withstand deformations in tension ($\epsilon_t$), compression ($\epsilon_c$), and shear ($\epsilon_s$) up to 30 m$\epsilon$, 20 m$\epsilon$, and 20 m$\epsilon$ respectively.

A finite-element (FE) model of the wing structure is created in NASTRAN [28] by discretising the composite-skins by quadrangular plate-elements and the internal foam by hexahedral volume-elements. A clamp boundary-condition is considered at the root section.

### 2.1 Design variables

Laminated composite plates are obtained by stacking different composite plies that, in the general framework, could have their own properties and thickness, as well as their own orientation. For this study, a single prototype ply is considered and the different stacks will only differ by the number and the orientation of the plies. The order in which the different plies are stacked is called *stacking-sequence*, that drives the mechanical behaviour of the laminate-plate. The latter can be locally expressed in the form of the constitutive law,

$$\begin{bmatrix} \mathbf{N} \\ \mathbf{M} \end{bmatrix} = \begin{bmatrix} \boldsymbol{A} & \boldsymbol{B} \\ \boldsymbol{B} & \boldsymbol{D} \end{bmatrix} \begin{bmatrix} \boldsymbol{\epsilon} \\ \boldsymbol{\kappa} \end{bmatrix} \tag{1}$$

**Table 1** Materials' properties

| | $E_{(1)}$ (GPa) | $E_{(2)}$ (GPa) | $\nu_{(12)}$ | $G$ (GPa) | $\rho$ kg/m$^3$ | $h_{ply}$ mm | $\epsilon_t$ m$\epsilon$ | $\epsilon_c$ m$\epsilon$ | $\epsilon_s$ m$\epsilon$ |
|---|---|---|---|---|---|---|---|---|---|
| Ply | 31.3 | 5.34 | 0.29 | 1.90 | 1727 | 0.17 | 30 | 20 | 20 |
| Foam | 0.095 | – | | | 0.30 | | 0.014 | | 80 |

where $\mathbf{N}$ and $\mathbf{M}$ are the local in-plane and bending loads applied to the composite stack and $\boldsymbol{\epsilon}$ and $\boldsymbol{\kappa}$ the local strains and curvatures of the plate [6, 29]. The relation between load and deformation is given by the stiffness matrix. This can be divided in: (i) $\boldsymbol{A}$ that describes the *membrane* behaviour, i.e. the direct link between $\mathbf{N}$ and $\boldsymbol{\epsilon}$; (ii) $\boldsymbol{D}$ that describes the *bending* behaviour, i.e. the direct link between $\mathbf{M}$ and $\boldsymbol{\kappa}$; (iii) $\boldsymbol{B}$ that couples the two behaviours. All these matrices are a function of the stacking sequence; in particular, $\boldsymbol{B} = \mathbf{0}$ when a symmetric stack is considered, as it is the case in this study.

The natural choice for the design variables would be the stacking-sequence itself. However, this poses some technical challenges, namely an optimisation with an undetermined number of variables, mixed continuous and discrete variables, and a non-smooth description of the functions of interest. A solution to this is given by the *lamination parameters* [30], i.e. a parameterisation of the stiffness matrix in Eq. 1 that is based on the homogenisation of the composite stack. The local properties of the material are hence described by the relations,

$$\begin{aligned} \boldsymbol{A} &= h \left(\boldsymbol{\Gamma}_0 + \boldsymbol{\Gamma}_1 \xi_1^A + \boldsymbol{\Gamma}_2 \xi_2^A + \boldsymbol{\Gamma}_3 \xi_3^A + \boldsymbol{\Gamma}_4 \xi_4^A\right) \\ \boldsymbol{D} &= \tfrac{h^3}{12} \left(\boldsymbol{\Gamma}_0 + \boldsymbol{\Gamma}_1 \xi_1^D + \boldsymbol{\Gamma}_2 \xi_2^D + \boldsymbol{\Gamma}_3 \xi_3^D + \boldsymbol{\Gamma}_4 \xi_4^D\right) \end{aligned} \tag{2}$$

where $\xi^A_{1,2,3,4}$ and $\xi^D_{1,2,3,4}$ are the lamination parameters for the membrane stiffness-matrix $\boldsymbol{A}$ and bending stiffness-matrix $\boldsymbol{D}$, $h$ is the total thickness of the laminate plate, and $\boldsymbol{\Gamma}_i$ are the Tsai-Pagano material parameters of the composite ply [29]. Using the lamination parameters as design variables enables to formulate the composite design problem as a continuous optimisation problem with a fixed number of variables, regardless of the actual number of plies of the laminates.

The design variables are hence defined as the total thickness $h$ and the 8 lamination parameters $\xi^A_{1,2,3,4}, \xi^D_{1,2,3,4}$; the homogenised properties of the laminated plate are considered uniform in each of the 10 design-zones in Fig. 1, resulting in a total of $(1 + 8) \times 10 = 90$ design variables. To ensure that the solutions are representative of actual laminates, compatibility conditions have to be enforced between the membrane and the bending lamination parameters as additional constraints to the optimisation [31]. Lower and upper limits are enforced on the laminate thickness for manufacturing and geometrical reasons: the total thickness $h$ is hence bounded between 1.70 mm (10 plies) and 3.74 mm (22 plies).

## 3 Aeroelastic design procedure

The goal of the design is to alleviate the static and dynamic loads on the wing, while respecting a prescribed flight-shape; this leads to specific choices on load-cases and optimisation strategy.

### 3.1 Load-cases and constraints

The considered load-cases span the typical sizing conditions for the aeronautic design (Table 2): a nominal cruise, a high load-factor condition and the response to gusts of variable time-scale. The asymptotic flow conditions are based on the ones expected in the wind-tunnel during the experiments; the Mach number $M$ is chosen to match the design condition for the CRM model and the other quantities are computed based on the hypothesis of an isentropic flow. Similarly, harmonic gusts are considered due to limitations of the experimental gust-generation apparatus.

The loads representing the cruise condition are based on high-fidelity simulations via the in-house ONERA solver elsA [32]. The aerodynamic mean-flow is computed for the scaled CRM geometry of the wing, here taken as reference flight-shape and the angle-of-attack of the wing have been tuned to match the typical cruise condition of a lift coefficient $C_L$ equal to 0.5. The retrieved pressure field is interpolated on the structural model—more precisely at the center of the plate-elements describing the composite skin—and, then, introduced as a pressure-load ($\mathbf{f}_{cruise}$). The jig-shape of the wing is updated at each outer iteration of the design loop to ensure that the flight-shape is met under the precomputed cruise loads, see Algorithm 1.

The *max-load* case, instead, takes into account the aeroelastic behaviour of the wing in the loads computation. The

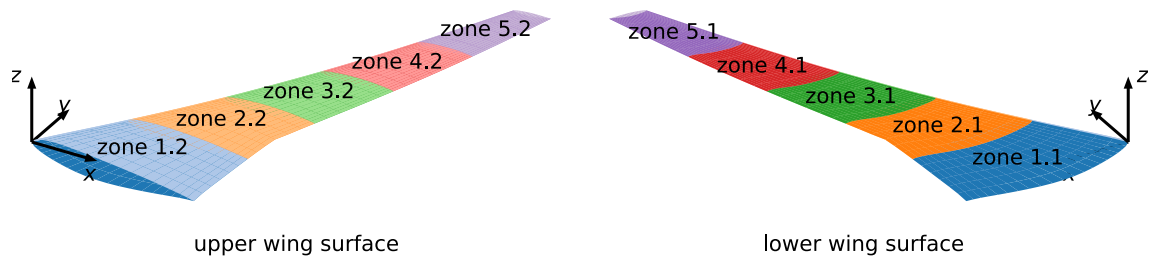


**Fig. 1** Wing-geometry and regions for the composite-optimisation

**Table 2** Load-cases and constraints for the design procedure

| | Cruise | Max-load | Gusts |
|---|---|---|---|
| Type | Static | Static | Equiv. static |
| Method | RANS solver (rigid flight-shape) | DLM + FE model (aeroelastic trim) | DLM + FE model (aeroelastic response) |
| Code | elsA | NASTRAN `[sol145]` | NASTRAN `[sol146+101]` |
| Conditions | $M = 0.85,\ q = 31.95$ kPa , and $U = 276$ m/s | | |
| | $c_L = 0.5$ | $c_L = 1.0$ | 5 *worst* cases |
| | $Re \approx 4 \times 10^4$ | | $\Delta\alpha_g = 0.25°$ |
| | | | $\{f_i\}_g = \{40, \ldots, 120\}$ Hz |
| Constraints | $-\epsilon_c/3 < \epsilon_{I,II} < \epsilon_t/3$ and $\epsilon_s^{max} < \epsilon_s/3$ | | |

doublets-lattice-method (DLM) is used as a model for the wing aerodynamic; a flat aerodynamic mesh is generated based on the form in plan of the wing and coupled to the structural FE model via the native tools available in MSC NASTRAN. Thanks to this aeroelastic model, the wing is trimmed, by acting on the angle of attack, to a lift coefficient equal to 1.0; this $C_L$ value is chosen to represent a $2g$-maneuver.

The same aeroelastic model is also used in the evaluation of the gust loads. These will be taken into account in the optimisation procedure as equivalent-static-loads [33]; this method allows to take into account dynamic load-cases as static loads, based on the dynamic simulation of the dynamic phenomenon of interest. In this work. harmonic gusts are considered: Fig. 2a, b report the fluctuations of the tip-displacement and the root-bending-moment forced by an harmonic gust of frequency $f = 75$ Hz and amplitude $\Delta\alpha = 0.25°$. From this response, the time $\bar{t}$ that maximises the tip displacement is chosen as sizing state; the full displacement field $\mathbf{x}'(\bar{t})$ is retrieved and the resulting equivalent-static-loads $\mathbf{f}$ are computed via the stiffness matrix of the complete structural model $\boldsymbol{K}$ as,

$$\mathbf{f} = \mathbf{f}_{cruise} + \boldsymbol{K}\,\mathbf{x}'(\bar{t}) \tag{3}$$

where the precomputed cruise-loads $\mathbf{f}_{cruise}$ are added to the fluctuation field. Thus, the forces calculated return, in a static simulation, a displacement field that will reproduce the dynamically computed gust response around the cruise condition. Only the gusts with the 5 largest tip-displacements are retained for the optimisation procedure, as reported in Fig. 2c, where it can be also noticed the change in phase-shift between tip-displacement and root-bending-moment when sliding in frequency. The choice of a limited number of gust cases for the computation of the static loads is necessary to limit the number of load cases during the optimisation. Nevertheless, the design is verified a-posteriori for all gust cases and all time steps, see Fig. 7.

Strain constraints are enforced; principal and maximal-shear strains are extracted at top and bottom of each

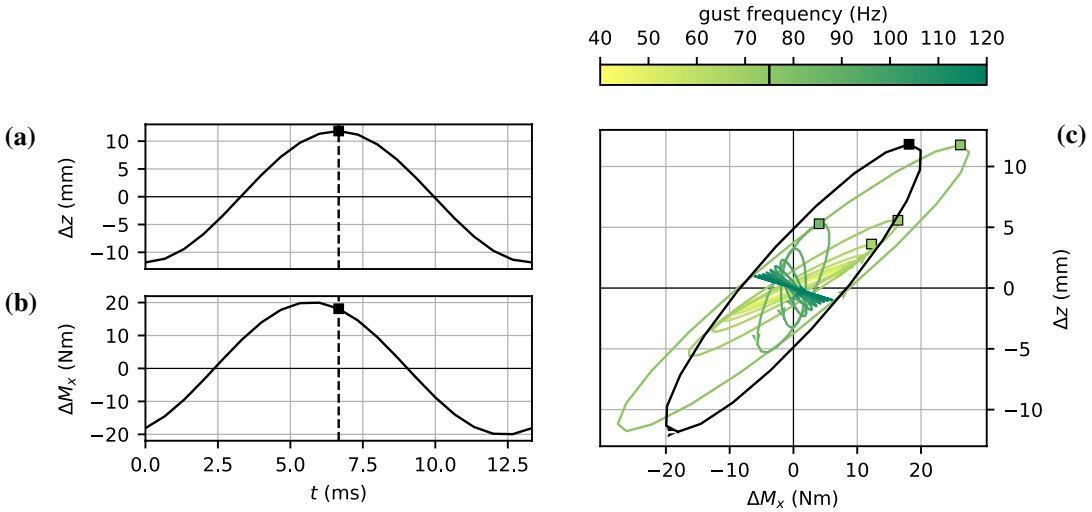


**Fig. 2** Harmonic gust response and sizing conditions. **a**, **b** report the fluctuation of tip-displacement and root-bending-moment for a gust at 75 Hz and amplitude $\Delta\alpha = 0.25°$. The time of maximum tip-displacement is chosen as sizing-condition (black-square). The black line in (**c**) report the phase-diagram representation of the response in (**a**, **b**); the colored lines report the same response for different gust frequencies. The squares indicate the retained sizing-cases

plate-element and limited by the values in Table 1, with a safety-factor 3. Since the ply orientations are unknown during the structural optimisation phase, the failure criterion is expressed in terms of the principal deformations of the laminate. The criterion defines the region of the deformation space that is safe regardless of the ply orientation [34]. In the present case, a simple maximum strain failure envelope is considered sufficient, thanks to the significant safety factors taken into account, but more accurate quadratic envelopes could be used within the same framework.

### 3.2 Optimisation method

The optimisation loop is described in Algorithm Algorithm 1 for the general objective function $J(\mathbf{p};\boldsymbol{\pi})$, where $\mathbf{p}$ is the vector containing the design variables and $\boldsymbol{\pi}$ the one for the optimisation parameters. At each step of the outer loop, the equivalent static loads are recomputed for the retained gust-cases and fed to the MSC NASTRAN built-in optimizer; once the solution that optimizes the general cost function $J$ has been found, the jig-shape is updated via the new stiffness matrix. This loop is repeated N times; in the last $M$ outer steps the thickness of the laminate-plates is fixed to an integer multiple of $2\,h_{ply}$ and only the lamination parameters are optimized. This improves, at least from a thickness point-of-view, the feasibility of the identified optimal-solution and it will facilitate the identification of the corresponding stacking-sequence in a second step.

The number of external steps $N$ is set to 10, with $M = 3$ rounded-thickness iterations.

**Algorithm 1** Design loop when minimising the generic cost function $J$

**for** $n \leftarrow 0$ **to** $N-1$ **do**

*Collect the equivalent-static-loads* $\{\boldsymbol{f}_i\}_g$ *for the gust cases* $\{f_i\}_g$
  **for all** $f_i \in \{f_i\}_g$ **do**
    *Solve the forced, aeroelastic problem*
    **solve** $\boldsymbol{M}\,\ddot{\boldsymbol{x}}' + (\boldsymbol{K}^{(n)} + \boldsymbol{K}_a(f_g;\, M))\,\boldsymbol{x}' = \Delta\alpha_g\,\boldsymbol{B}_g\,\cos(f_g t/2\pi)$ ▷ `[sol146]`
    *Identify the critical-time when the tip displacement is maximal*
    $\bar{t} \leftarrow \max_t z'_{tip}(t)$
    *Compute the equivalent static loads*
    **return** $\boldsymbol{f}_i \leftarrow \boldsymbol{f}_{cruise} + \boldsymbol{K}^{(n)}\,\boldsymbol{x}'(\bar{t})$ ▷ `[sol101]`
  **end for**

  **if** $n \leq N - M$ **then**
    $\boldsymbol{p} \coloneqq \{\{h, \xi^A_{1,2,3,4}, \xi^D_{1,2,3,4}\}_i\} \quad \boldsymbol{\pi} \coloneqq \{\boldsymbol{\Gamma}_0, \boldsymbol{\Gamma}_1, \boldsymbol{\Gamma}_2, \boldsymbol{\Gamma}_3, \boldsymbol{\Gamma}_4\}$
  **else**
    *Round the thickness to the closest integer multiple of* $2h_{ply}$
    **for all** $h \in \{h_i\}$ **do**
      $h \leftarrow 2h_{ply} \times \text{round}\left(h/2h_{ply}\right)$
    **end for**
    *Re-define the design variables to lamination parameters only*
    $\boldsymbol{p} \coloneqq \{\{\xi^A_{1,2,3,4}, \xi^D_{1,2,3,4}\}_i\} \quad \boldsymbol{\pi} \coloneqq \{\{h\}_i, \boldsymbol{\Gamma}_0, \boldsymbol{\Gamma}_1, \boldsymbol{\Gamma}_2, \boldsymbol{\Gamma}_3, \boldsymbol{\Gamma}_4\}$
  **end if**

  *Composite material optimisation*
  **minimise** $J(\boldsymbol{p};\, \boldsymbol{\pi})$ ▷ `[sol200]`
    loads and constraints: Table 2 + compatibility conditions for $\xi_i^{(\cdot)}$
  **return** $\boldsymbol{p}$

  *Update jig-shape*
  $\boldsymbol{x}_{jig}^{(n+1)} \leftarrow \boldsymbol{x}_{cruise} - \boldsymbol{K}^{(n+1)^{-1}}\,\boldsymbol{f}_{cruise}$ ▷ `[sol101]`

**end for**

When NASTRAN is used in a step, the solution type is reported in squared brackets.

## 4 Bi-objective optimisation: a trade-off between static and dynamic behaviours

The choice of the cost function $J$ drives the optimisation; since the aim is the alleviation of both static and dynamic aeroelastic loads on the wing, a bi-objective strategy is pursued. On the static side, the objective is to minimise the root-bending-moment for the max-load case and, by this, to alleviate the structural loads when an off-cruise condition is encountered. On the dynamic side, an ensemble measurement of the response to the harmonic gusts is considered: this is quantified by the root-mean-squared of the tip-displacement on the retained gust-loads.

Figure 3 reports the Pareto front obtained for these two objective functions. The boundaries for the two objective functions are calculated by performing two separated design procedures using the aforementioned static (vertical dashed line) and dynamic (horizontal dashed line) objectives. These lines represent the minimal values that the two objectives can present for a sized wing and, hence, the left and bottom limits for the points that trace the Pareto front. The latter is obtained via an $\epsilon$-constrained method [35], which consists in a series of consecutive optimisations for one of the cost functions—in this case, the gust response—while the other one—the root-bending-moment—is constrained to be lower than a certain value. In this manner, the Pareto front can be covered by computing the consecutive optimal points for the first (and free) objective, for increasing values of the second (and constrained) one. So that this strategy works, the two cost-functions are required to be antagonist to each other, condition that is verified for this choice of objective functions.

The jig-shape is computed as part of the optimisation procedure; Fig. 4a shows how the twist-angle along the span coordinate $y$ changes for the different points of the Pareto front. The distance between flight-shape and jig-shape is an indication of the overall flexibility of the wing, the larger the distance the more flexible the structure. Stiffer solutions are also heavier, and they are characterised by a larger root-bending-moment; as the flexibility increases, the wing becomes lighter, the root-bending-moment decreases at the cost of an increased gust-response.

Note that each point of the Pareto front respects the considered combination of structural constraints and load cases. The trade-off between static and dynamic performances is possible by allowing a penalty on the overall mass of the wing that, since we are designing a wing-tunnel model, is not critical for our application. The mass-penalty is computed and reported by the color-scale with respect to a reference design, i.e. the minimal-mass design (white square). The latter is computed by following the same optimisation procedure described in Algorithm 1 with the overall mass of the wing as objective.

### 4.1 Final design

In a bi-objective optimisation, the definition of an unique design-point requires to arbitrarily pick a *best compromise* between the two objectives of the Pareto front; in this work, the jig-shape is considered as a criterion for this choice. Figure 4b resumes the information in Fig. 4a and shows the twist at the wing-tip and the span-wise twist-range as a function of the root-bending-moment. The *flattest* jig-shape—i.e. the one with the most limited variation of twist angle between root and tip—can be identified and chosen as the final design-point, light-blue square in Fig. 3 and 4b. This choice is dictated by practical aspects related to the manufacturing process and it is aimed to facilitate the fabrication of the molds used to lay the composite laminates.

The value of the design variables at chosen design-point are visualised in Fig. 5; the color-scale reports the local

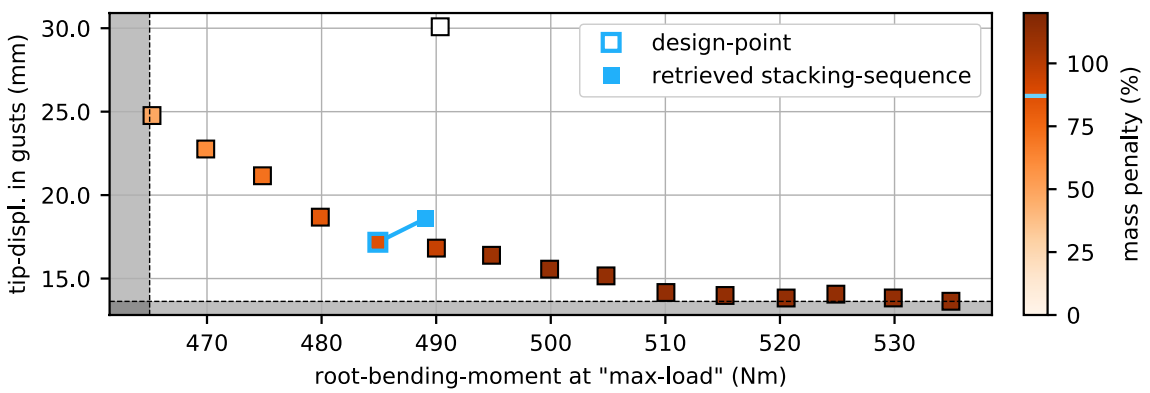


**Fig. 3** Pareto front. The colour-scale report the mass penalty with respect to the optimal-mass solution, here in white. The light-blue contoured point is the selected design-point, while the light-blue square reports the performance of the retrieved stacking-sequence (see Sect. 5 and Fig. 8). The optimal limits for the two cost functions are reported by the shaded areas

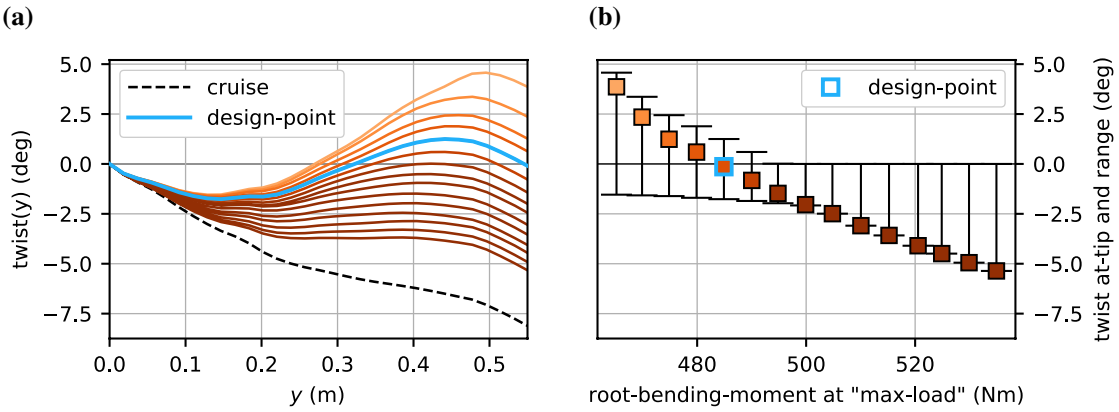


**Fig. 4** Design-point criterion.The jig-shape twist is reported in (**a**) for each point of the Pareto-front in Fig. 3. The squares in (**b**) report the twist angle at the wing-tip as a function of the root-bending-moment, while the error-bars indicate the variation range of the twist along the span-wise direction

thickness of the laminate plate, while the polar-plots are a representation of the in-plane anisotropy of the constitutive law, i.e. how the stiffness of the base-ply is redistributed by the lamination parameters. This visualisation reports the engineering modulus,

$$E(\theta) = \frac{1}{\left(\boldsymbol{T}(\theta)^{-1}\boldsymbol{A}^{-1}\boldsymbol{T}(\theta)\right)_{11}} \tag{4}$$

where $\theta$ is the polar angle, $\boldsymbol{A}$ is the membrane tensor, and $\boldsymbol{T}(\theta)$ is the rotation operator for the deformation vector $\boldsymbol{\epsilon}$ [8]; the subscript indicates which element of the tensor is considered—first row and first column, in this case. The red lines in Fig. 5 report the engineering modulus, while the blue ones a corresponding quantity computed for the flexion tensor $\boldsymbol{D}$. The overall membrane-stiffness is oriented as the wing sweep; the misalignment occurs either for the flexion tensor or for marginal redistribution of the membrane-stiffness in the root region.

Further insight in the design process can be given by the constraints, since different wing regions are sized by different load-cases; Fig. 6 shows, for each element, which load-case pushes the evaluated strains the closest to the constraint boundary. Two load cases rise from this analysis; the max-load that sizes the root-to-kink region and the 75 Hz gust that interests the rest of the wing. The first one only activates the constraints in a few elements in the kink region. The second one, instead, affects the tip region, but with a constraint far from being activated; this is due to the imposed technological limit of a minimum of 10 plies that clearly oversizes the structure for strain constraint. It has to be noticed that this analysis returns only a view on the sizing

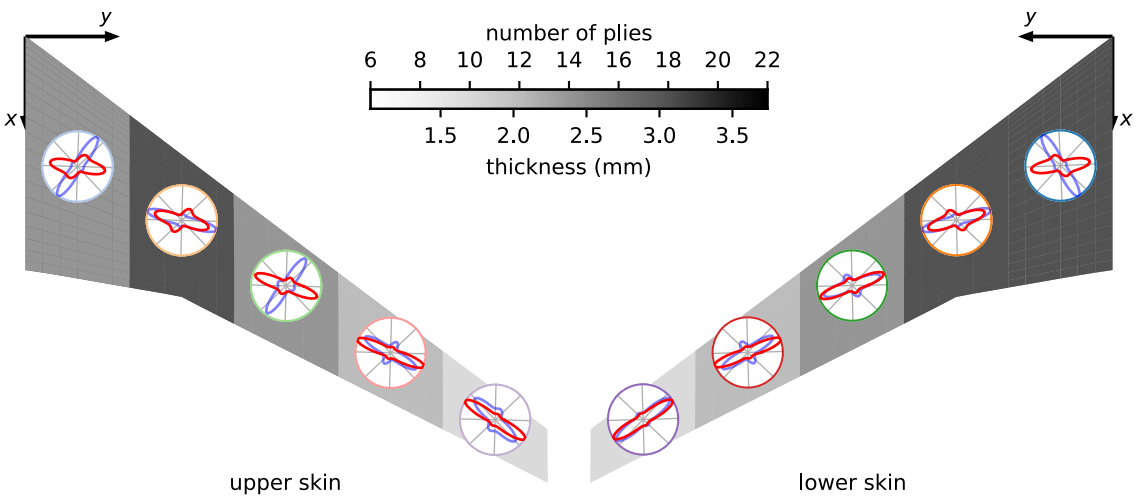


**Fig. 5** Design point. The design variables—thickness and composite properties—are reported; the material properties are represented via the polar-plot of the engineering modulus, in red for the membrane-stiffness ($\boldsymbol{A}$ tensor) and in blue for the flexion one ($\boldsymbol{D}$ tensor)

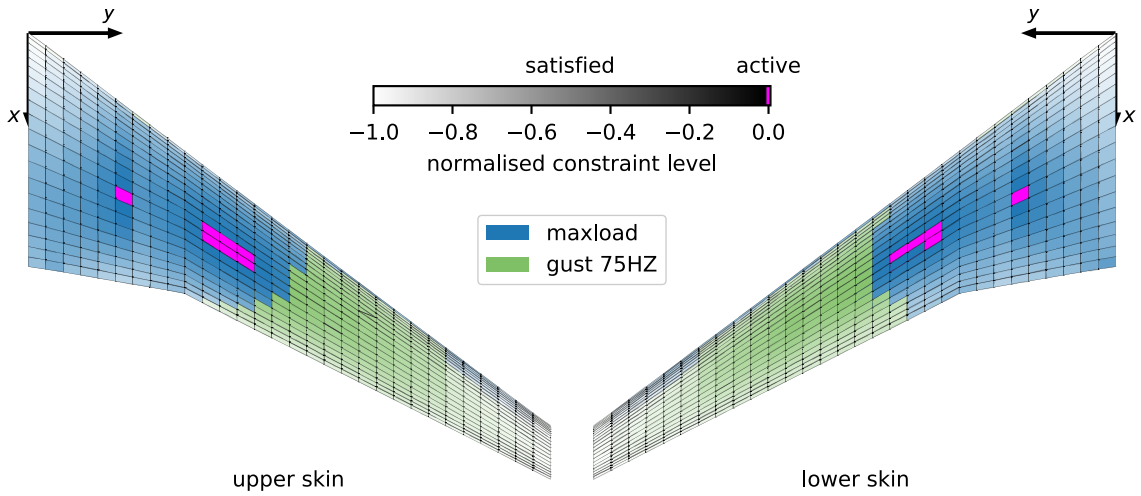


**Fig. 6** Sizing load-cases. The colour shows, for each element of the model, the load case that pushes the strains the closest to the failure envelope. The saturation indicates the proximity to the boundary; if the constraint is *active*—i.e. it is on the boundary within a normalised constraint value of $5 \times 10^{-3}$—the element is coloured in magenta

by strain-constraint and it does not allow an insight of the role played by the load-cases in the objective-functions, of a more *global* nature.

The structural integrity of the design has been also verified on a more extended set of load-cases with respect to the ones considered in the optimisation (Fig. 7). The maxima of principal and maximal-shear strains are reported for the static load-cases, as well as for all the investigated gust responses. For the latter, the hypothesis of correlation between the maximal tip-displacement and the maximal load/strain is abandoned: the reported strain maxima are evaluated over one cycle of the harmonic gust response, i.e. the critical values is computed over all the time-steps of the simulations. It can be seen that the design respects the imposed limits (vertical lines) for all the load-cases considered in the verification process.

## 5 Towards manufacturing

Up to this point, the constitutive law describing the laminate plates have been described via the lamination parameters, as introduced in Sect. 2.1. This description allows for an easier implementation of the optimisation algorithm but, on the other hand, it does not give the information needed to manufacture the laminate-plate; the stacking-sequence has thus to be recovered from the homogenised description by the lamination parameters. This task—called *inverse problem*—is a crucial point of the design procedure and, most importantly, its solution could be not unique (see for instance [36]). Such multi-level optimisation framework is typical for laminated composite structures. In the following, we use a stiffness matching approach, i.e. the second-level optimisation aims at finding the laminates that best match the optimal stiffness from the first-level continuous optimisation [11].

The inverse problem is here solved by a second optimisation via a specialised evolutionary algorithm based on the work by [37]; Fig. 8 shows the identified stacking-sequence

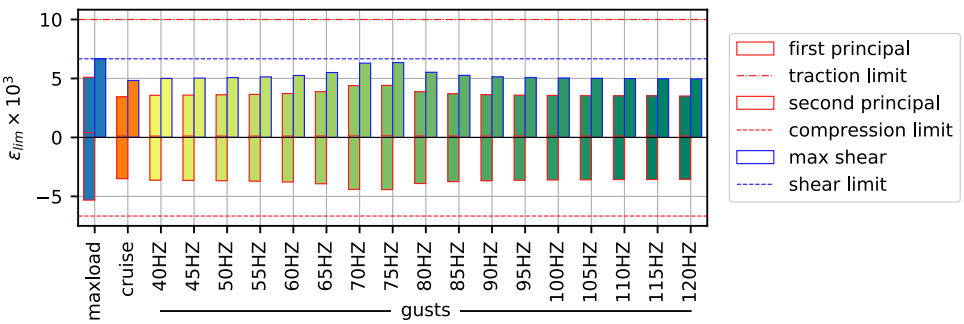


**Fig. 7** Verification of strain constraints at the design point. The different bars report the maxima of principal and maximal-shear strains registered both in the static (maxload and cruise) and dynamic (gusts) cases. The horizontal lines show the considered limits in the optimisation process

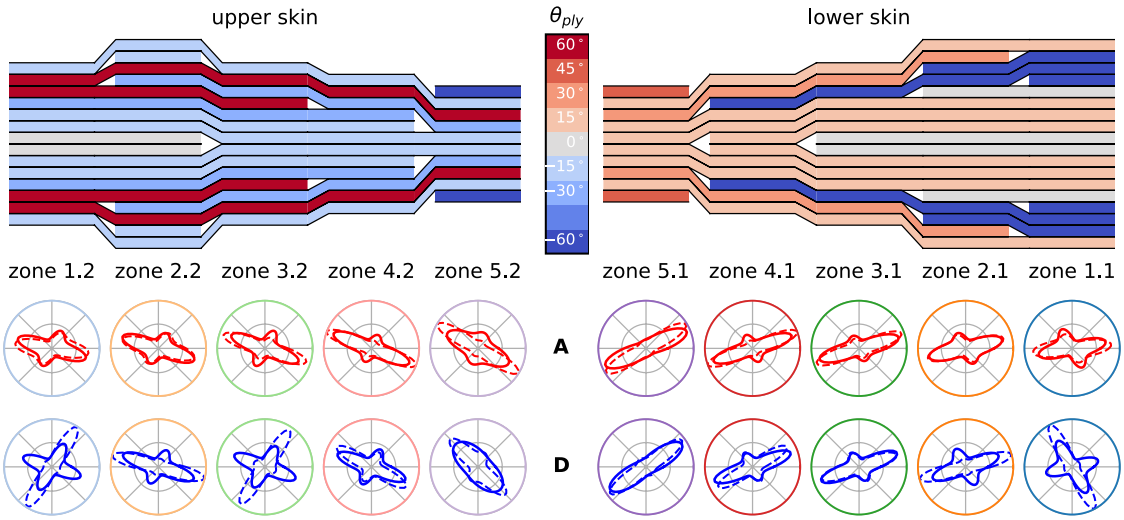


**Fig. 8** Stacking-sequence for the upper (left) and the lower (right) skin. The bottom part of the figure shows, for the membrane and flexion tensors $\boldsymbol{A}$ and $\boldsymbol{D}$, the deviation between the material properties prescribed by the continuous optimisation (dashed lines) and the properties for the retrieved stacking-sequence (solid lines)

for the upper and lower skin; the gap between the design-point (dashed lines) and the retrieved stacking-sequence (solid lines) is minimised but it is still present. This is mainly due to the manufacturing constraints taken into account in the optimisation: (i) ply angles are allowed to take value in the set $\{-60, -45, ..., 90\}$ and the ply thickness is fixed, which defines a discrete sampling of the design space; (ii) ply-continuity, or *blending*, is imposed between the regions

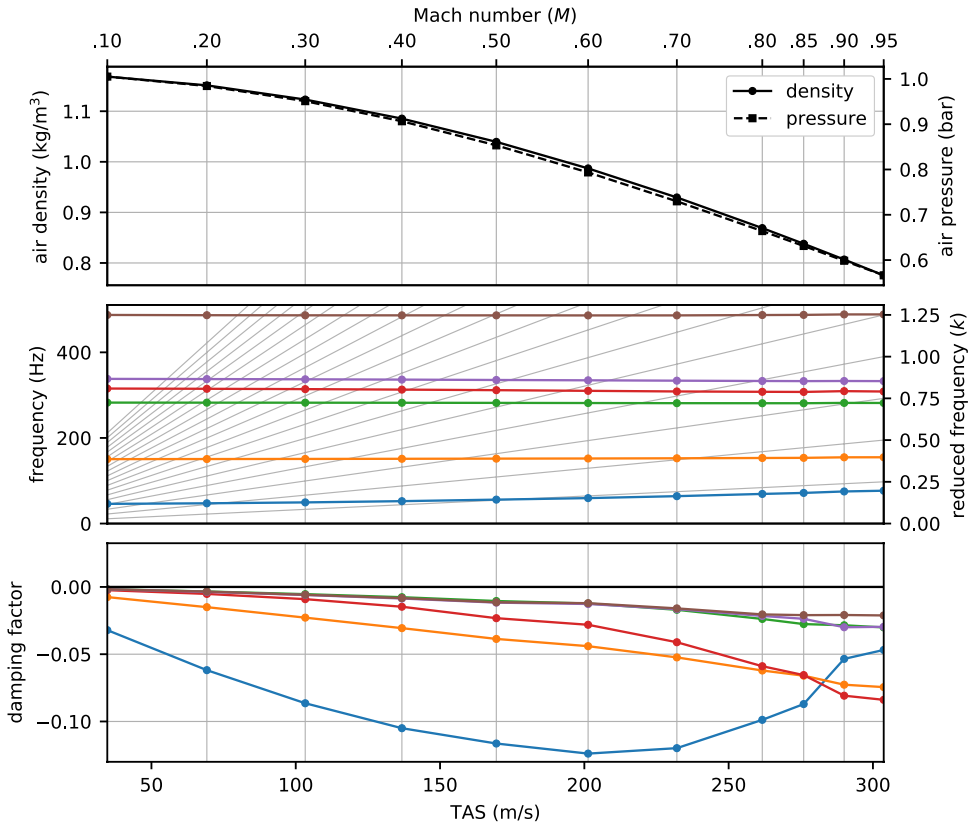


**Fig. 9** Flutter analysis of the final design. The top figure reports the flow condition for each flutter point. The two bottom figures, instead, show the results of the flutter analysis, i.e. frequency and damping-factor for the considered aeroelastic modes

to avoid strength-related issues. This significantly reduces the design space of the discrete optimisation with respect to the design space of the continuous optimisation. Indeed, all laminates are coupled due to the ply-continuity constraints, whereas they are assumed to be independent in the continuous optimisation. Recent studies —unfortunately not available at the time of the finalisation of the design— investigated the possibility of taking into account the *blending* problem by introducing additional constraints already at the stage of the lamination-parameter optimisation [38].

The performance registered by the identified stacking-sequence are reported on the Pareto front in Fig. 3 by the filled light-blue square; the root-bending-moment at max-load is higher as the gust response but it places in the vicinity of the design-point. Since the thickness of the composite skins is conserved by the algorithm solving the inverse problem, the mass of the wing is unaltered. All the strain constraints have been verified for the retrieved stacking-sequence.

Moreover, a flutter analysis has been conducted by means of a FEM-DLM analysis and the wing results flutter-stable up to Mach 0.95, Fig. 9. The flow condition—reported in the top figure—are set to mimic the wind-tunnel behaviour during the planned tests; the stagnation state of the gas ($\rho_0 = 1.225$ kg/m$^3$, $p_0 = 1.013$ bar) is fixed and the static density ($\rho$) and pressure ($p$) are computed by the isentropic flow relations

$$p = p_0\left(1 + \frac{\gamma - 1}{2}M^2\right)^{\frac{\gamma}{1-\gamma}} \quad \text{and} \quad \rho = \rho_0\left(1 + \frac{\gamma - 1}{2}M^2\right)^{\frac{1}{1-\gamma}} \tag{5}$$

where $M$ is the Mach number and $\gamma$ the specific heat ratio. The two bottom figures report the results of the flutter analysis as a function of the Mach number and the true-air-speed (TAS); all the damping coefficients are negative for all the considered analysis points, indicating that the wing is flutter-stable across the conditions to be found during the experimental campaign.

## 6 Conclusions

A complete aeroelastic-tailoring method is presented and, thus, applied to design composite wing to alleviate both static and dynamic aeroelastic loads. Its structure is built from two composite-skins each divided in 5 design-regions, where thickness and laminate properties—parameterised via the lamination-parameters formalism—are optimized.

A bi-objective optimisation is performed, based on the performance in a high-load condition and in gust. The design process takes into account 7 load-cases; the nominal cruise, the high-load condition, and 5 load-cases representing the response to harmonic gusts at different frequencies. Among the multiple optimal-designs identified in the form of a Pareto front, the final design-point is chosen via a criterion on the jig-shape.

As final step of a bi-step design-strategy, the stacking-sequences are retrieved for the identified design-point via a specialised evolutionary algorithm. The performance and constraints of the discrete, manufacturable solutions are verified and compared with the continuous optimum.

The here-presented design has been manufactured at DLR and wind-tunnel experiments took place at ONERA in 2021 to validate its performance against the numerical simulations. The data from the experimental campaign will be soon available to the aeroelastic community.

**Acknowledgements** The authors would like to acknowledge Fabien Huvelin for the RANS simulations in cruise condition and Christophe Blondeau and Marco Tito Bordogna for the fruitful discussions and collaboration. The present work is part of the Common Research Project FIGURE—a collaboration between ONERA and DLR—and internal ONERA's research project CARACAL.This publication is an extension of the work that was previously presented at the Aerospace Europe Conference (AEC) 2021 organised by CEAS in Warsaw (Poland).

## References

1. Shirk, M.H., Hertz, T.J., Weisshaar, T.A.: Aeroelastic tailoring—theory, practice, and promise. J. Aircr. **23**(1), 6–18 (1986)
2. Munk, M.: Propeller Containing Diagonally Disposed Fibrous Material. U.S. Patent 2,484,308,1111 (1949)
3. Jutte, C.V., Stanford, B.K.: Aeroelastic tailoring of transport aircraft wings: State-of-the-art and potential enabling technologies. Technical Report NASA/TM-2014-218252, NASA (2014)
4. Venkataraman, S., Haftka, R.T.: Optimization of Composite Panels. A Review (1999)
5. Arizono, H., Isogai, K.: Application of genetic algorithm for aeroelastic tailoring of a cranked-arrow wing. J. Aircr. **42**(2), 493–499 (2005)
6. Tsai, S.W., Hahn, T.H.: Introduction to Composite Materials. Technomic Publishing Company, Lancaster (1980)
7. Verchery, G.: Les invariants des tenseurs d'ordre 4 du type de l'aélasticité. In: Boehler, J.-P. (ed.) Mechanical Behavior of Anisotropic Solids / Comportment Méchanique des Solides Anisotropes, pp. 93–104. Springer, Dordrecht (1982)
8. Dillinger, J.K.S.: Static aeroelastic optimization of composite wings with variable stiffness laminates. Phd thesis, TU Delft, The Netherlands (2014)
9. Rajpal, D., Gillebaart, E., Breuker, R.D.: Preliminary aeroelastic design of composite wings subjected to critical gust loads. Aerosp. Sci. Technol. **85**, 96–112 (2019)
10. Sigmund, O.: Materials with Prescribed Constitutive Parameters: An Inverse Homogenization Problem (1994)
11. Irisarri, F.-X., Julien, C., Bettebghor, D., Lavelle, F., Guerin, Y., Mathis, K.: A general optimization strategy for composite sandwich structures. Struct. Multidisc. Optim. **63**, 3027–3044 (2021)
12. Scarth, C., Cooper, J.E.: Reliability-based aeroelastic design of composite plate wings using a stability margin. Struct. Multidisc. Optim. **57**, 1695–1709 (2018)
13. Nitschke, C., Vincenti, A., Chassaing, J.-C.: Influence of stochastic perturbations of composite laminate layups on the aeroelastic

flutter of a cantilevered plate wing. Compos. Struct. **220**, 809–826 (2019)
14. Albano, E., Rodden, W.P.: A doublet-lattice method for calculating lift distributions on oscillating surfaces in subsonic flows. AIAA J. **7**(2), 279–285 (1969)
15. Morino, L., Bharadvaj, B.K., Freedman, M.I., Tseng, K.: Boundary integral equation for wave equation with moving boundary and applications to compressible potential aerodynamics of airplanes and helicopters. Comput. Mech. **4**, 231–243 (1989)
16. Kenway, G., Kennedy, G., Martins, J.R.R.A.: Aerostructural optimization of the common research model configuration. In: 15th AIAA/ISSMO MDAO Conference, Atlanta, Georgia (2014)
17. Achard, T., Blondeau, C., Ohayon, R.: High-fidelity aerostructural gradient computation techniques with application to a realistic wing sizing. AIAA J. **56**(11), 4487–4499 (2018)
18. Jonsson, E., Riso, C., Monteiro, B.B., Gray, A.C., Martins, J.R., Cesnik, C.E.: High-fidelity gradient-based wing structural optimization including a geometrically nonlinear flutter constraint. In: AIAA SCITECH 2022 Forum, San Diego, California (2022)
19. Neumann, J., Mai, H.: Gust response: simulation of an aeroelastic experiment by a fluid-structure interaction method. J. Fluids Struct. **38**, 290–302 (2013)
20. Lepage, A., Amosse, Y., Bihan, D.L., Poussot-Vassal, C., Brion, V., Rantet, E.: A complete experimental investigation of gust load: from generation to active control. In: IFASD 2015-International Forum on Aeroelasticity and Structural Dynamics (2015)
21. Brion, V., Lepage, A., Amosse, Y., Soulevant, D., Senecat, P., Abart, J.C., Paillart, P.: Generation of vertical gusts in a transonic wind tunnel. Exp. Fluids **56**, 145 (2015)
22. Geeraert, A., Lepage, A., Stephani, P., Feldmann, D., Häberli, W.: Wind tunnel flutter tests of a U-tail configuration - Part 1: Model design and testing. In: IFASD 2017-International Forum on Aeroelasticity and Structural Dynamics (2017)
23. Meddaikar, M.Y., Dillinger, J., Ritter, M.R., Govers, Y.: Optimization & testing of aeroelastically-tailored forward swept wings. In: IFASD 2017-International Forum on Aeroelasticity and Structural Dynamics (2017)
24. Merienne, M.-C., Molton, P., Bur, R., Le Sant, Y.: Pressure-sensitive paint application to an oscillating shock wave in a transonic flow. AIAA J. **53**(11), 3208–3220 (2015)
25. Molton, P., Le Sant, Y., Carpels, Y., Beck, W., Klein, C., Henne, U., Sachs, W.: Benchmark testing of ONERA and DLR pressure sensitive paints for unsteady/instationary flows. In: MOTAR DLR/ONERA Cooperation (2016)
26. Le Sant, Y., Mignosi, A., Deléglise, B., Bourguignon, G.: Model deformation measurement (MDM) at ONERA. In: $25^{th}$ AIAA Applied Aerodynamics Conference (2007)
27. Common Research Model. Website: page last modified on September 10, 2019. https://commonresearchmodel.larc.nasa.gov/
28. MSC Software: MSC Nastran 2018 Design Sensitivity and Optimization User's Guide. (2017)
29. Tsai, S.W., Pagano, N.J.: Invariant properties of composite materials. In: Tsai, S.W., Halpin, J.C., Pagano, N.J. (eds.) Composite Materials Workshop, St. Louis, Missouri, 1967, pp. 233–253. Technomic Publishing Company, Lancaster (1968)
30. Miki, M., Sugiyama, Y.: Optimum design of laminated composite plates using lamination parameters. AIAA J. **31**(5), 921 (1993)
31. Diaconu, C.G., Sekine, H.: Layup optimization for buckling of laminated composite shells with restricted layer angles. AIAA J. **42**(10), 2153–2163 (2004)
32. Cambier, L., Heib, S., Plot, S.: The ONERA elsA CFD software: input from research and feedback from industry. Mech. Ind. **4**(3), 159–174 (2013)
33. Park, G.-J.: Technical overview of the equivalent static loads method for non-linear static response structural optimization. Struct. Multidisc. Optim. **43**, 319–337 (2011)
34. Khani, A., IJsselmuiden, S.T., Abdalla, M.M., Gurdal, Z.: Design of variable stiffness panels for maximum strength using lamination parameters. Compos. Part B: Eng. **42**(3), 546–552 (2011)
35. Haimes, Y.V., Lasdon, L.S., Wismer, D.A.: On a bicriterion formation of the problems of integrated system identification and system optimization. IEEE Trans. Syst., Man, Cybern. Syst. SMC-1(3), 296–297 (1971)
36. Vannucci, P., Verchery, G.: Stiffness design of laminates using the polar method. Intl. J. Solids Struct. **38**(50–51), 9281–9294 (2001)
37. Irisarri, F.-X., Lasseigne, A., Leroy, F.-H., Le Riche, R.: Optimal design of laminated composite structures with ply drops using stacking sequence tables. Compos. Struct. **107**, 559–569 (2014)
38. Bordogna, M.T., Lancelot, P., Bettebghor, D., De Breuker, R.: Static and dynamic aeroelastic tailoring with composite blending and manoeuvre load alleviation. Struct. Multidisc. Optim. **61**, 2193–2216 (2020)